Journal of Microscopy, Vol. 202, Pt 2, May 2001, pp. 339–346.
Received 28 August 2000; accepted 11 October 2000

Three-dimensional analysis of light propagation through uncoated near-field fibre probes

R. MÜLLER & C. LIENAU
Max-Born-Institut für Nichtlineare Optik und Kurzzeitspektroskopie, Max-Born-Str. 2A, D-12489 Berlin, Germany

Key words. Fibre probes, NSOM.

Summary

The near-field emission from uncoated tapered fibre probes is investigated for different probe geometries. The three-dimensional model calculations are based on Maxwell's curl equations and describe the propagation of a 10 fs optical pulse ($\lambda = 805$ nm) through tapers of different lengths and different diameters of the taper exit. The numerical evaluation is done with a finite difference time domain code. Two tapers with cone angles of 50°, with taper lengths of 1.5 μm and 1.0 μm and exit diameters of 100 nm and 520 nm, respectively, are considered. We find that without sample the short taper with large exit diameter optimizes both light transmission and spatial resolution. In the presence of a sample with a high dielectric constant, however, the spatial near-field distribution changes drastically for both taper geometries. We find a pronounced increase in spatial resolution, down to about 250 nm inside the medium. This collimation of the near-field distribution arises from interferences between emitted and reflected light from the sample surface and from a collimation effect that the field experiences in the high-index semiconductor material. The combination of high spatial resolution and transmission and collection efficiencies makes such probes interesting for spectroscopic investigations, as demonstrated by recent experiments.

1. Introduction

There is currently considerable experimental and theoretical interest in characterizing the local optical properties of novel low-dimensional semiconductor nanostructures such as quantum wells, wires and dots on nanometre length scales. Near-field scanning optical microscopy (NSOM) combined with highly spectrally and/or temporally resolved spectroscopic techniques presents a promising experimental approach as it permits imaging and spectroscopy on submicrometre length scales (Hess *et al.*, 1994; Richter *et al.*, 1997; Toda *et al.*, 1999). So far, most of the experimental work on technologically relevant III/V semiconductor nanostructures has been performed with metal-coated aperture probes. The investigated layered subsurface nanostructures are generally embedded in high refractive index barrier materials and buried by typically 50–100 nm below the sample surface. Thus, the optical resolution in these experiments is not limited by the diameter of the aperture probe but rather by the considerably enhanced width of the electromagnetic field distribution at the depth of the nanostructure layer. Indeed, in most spectroscopic semiconductor nanostructure studies the reported resolution was in the range 150–250 nm. Careful experiments on single quantum dots buried by 70 nm were performed by Saiki & Matsuda (1999) with specifically optimized metal-coated aperture probes. These experiments showed that even for apertures of less than 100 nm diameter the resolution in illumination/collection mode PL experiments was limited to about 150 nm.

As is well known, a reproducible fabrication of such metal-coated aperture probes is non-trivial and such probes possess several drawbacks such as low throughput, low damage threshold and sometimes shadowing effects that arise from the metal coating. There thus appears to be a need for complementary techniques which achieve similar spatial resolution. Recently, Wu *et al.* (1999) imaged the near-infrared emission (at a wavelength of $\lambda = 730$ nm) of localized excitons in thin GaAs quantum wells with 250 nm or $\lambda/3$ spatial resolution using solid immersion lens microscopy. Even higher resolution was recently reported in spectroscopic experiments with uncoated tapered single mode optical fibres. Von Freymann *et al.* (2000) imaged single defects in ZnSe quantum wells at $\lambda = 440$ nm with 200 nm resolution. Lewis *et al.* (1998) achieved 175 nm resolution in femtosecond two-photon spectroscopy of rhodamine B molecules at $\lambda = 800$ nm. Guenther *et al.* (1999) demonstrated 200 nm resolution in femtosecond pump-probe experiments on single quantum wires. In

Correspondence to: Roland Müller. Tel.: +49 30 6392 1448; fax: +49 30 6392 1489; e-mail: rmueller@mbi-berlin.de

an illumination/collection geometry, Intonti *et al.* (2001) achieved 160 nm resolution at $\lambda = 745$ nm, corresponding to $\lambda/4.5$ in luminescence experiments on single quantum wires – very close to the resolution achieved with metal-coated probes (Saiki *et al.*, 1999). Intonti *et al.* (2001) also demonstrated that the transfer function of their microscope in this illumination/collection geometry was well described by a Gaussian profile. It is safe to assume that in all these experiments the truly spectroscopic contrast is free from topographic artefacts (Hecht *et al.*, 1997; Sandoghdar *et al.*, 1997)

Such uncoated fibre probes are currently in widespread use by many experimental groups and have significant advantages over metal-coated aperture probes. Reproducibly fabrication is achieved by using various etching techniques (Lambelet *et al.*, 1998; Saiki *et al.*, 1999; Stöckle *et al.*, 1999). The probes are characterized by very high transmission and collection efficiencies close to unity and damaging and shadowing problems are considerably reduced. This makes them highly interesting, in particular for nonlinear spectroscopy of subsurface nanotructures.

During the last few years there has been an intense, partly controversial, theoretical discussion about the resolution limit that may be obtained with uncoated fibre tips. Buckland *et al.* (1993) highlighted that in a strongly guiding, non-tapered, glass/air dielectric waveguide, a minimum field width of the guided HE_{11} mode of about $\lambda/2$ is obtained for a core radius/wavelength ratio of about 0.25. Novotny *et al.* (1995) calculated the field distribution in a tapered dielectric probe with a sharply pointed end (radius of curvature on the order of 10 nm). They found a minimum lateral width of the intensity distribution at a core radius/wavelength ratio of about 0.25, i.e. roughly 400 nm above the end of the taper. Further down the taper the light leaks out of the waveguide and thus the optical resolution at the taper end is predicted to be poor. Bozhevolnyi & Vohnsen (1997) carried out two-dimensional simulations of the field distribution in different trapezoidal fibre tips. The field distributions at the exit of the fibre tip show a rather complicated spatial structure with only a weak central peak with a width of 150 nm. None of these simulations predict the narrow Gaussian-shaped transfer function observed in the experiments cited above.

If polarization-resolved detection is introduced as an additional contrast mechanism recent experimental and theoretical studies prove that subwavelength resolution of $\lambda/4$ or possibly even lower can be obtained in an illumination/collection geometry with uncoated tapered fibre probes (von Freymann *et al.*, 1998; Adelmann *et al.*, 1999; Bozhevolnyi *et al.*, 1999).

It is the aim of this paper to demonstrate theoretically that the transmission properties of uncoated tapered optical fibre probes are strongly modified if a high refractive index medium, such as a semiconductor nanostructure, is brought into the near-field of the probe tip. This tip–sample interaction collimates the intensity distribution inside the medium and increases the spatial resolution down to about $\lambda/3.5$. The calculated transfer functions for such a tip/medium geometry are in good agreement with the recently reported experimental observations (Lewis *et al.*, 1998; Günther *et al.*, 1999; Intonti *et al.*, 2001) and highlight the potential of such probes for high spatial resolution linear and nonlinear optical spectroscopy of semiconductor nanostructures.

2. The model

Our simulations are based on a three-dimensional model of a fibre taper being rotationally symmetric around the z-axis (Fig. 1). Figure 1 also illustrates the used cylindrical coordinate system (r, ϕ, z) and Cartesian coordinates (x, y, z). The entrance and exit of the taper are indicated

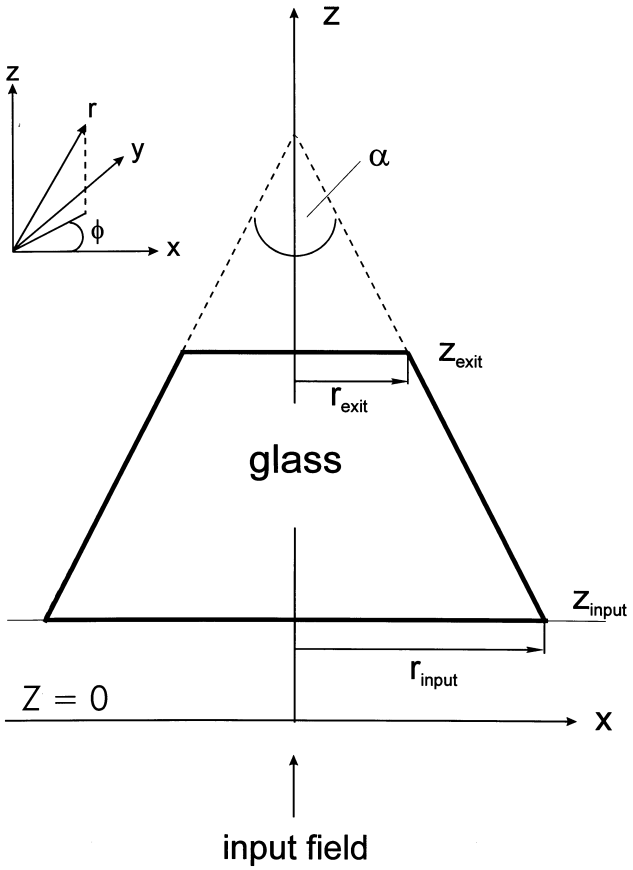

Fig. 1. Cross-section through a fibre taper being rotationally symmetric around the z-axis; z_{input}, r_{input} and z_{exit}, r_{exit} are the z coordinates and the radii of the taper at its entrance and exit, respectively. α is the cone angle of the taper. Numerical values for these parameters are found in the text. The input light field is a 10 fs pulse, polarized along the *x*-axis, which propagates in the z direction.

by z_{input} and z_{exit}, while r_{input} and r_{exit} denote the respective radii of the taper. α is its cone angle. At $z = z_{input}$, the fibre is assumed to be surrounded by a thin metal film to restrict the incident field to the taper dimension. Throughout the paper, the following parameters characterize the taper: $\alpha = 50°$, $z_{input} = 0.5$ μm, $r_{input} = 0.8$ μm, while different values will be used for z_{exit} and r_{exit}.

The electric and magnetic field components are given by (E_r, E_ϕ, E_z) and (H_r, H_ϕ, H_z),respectively. Light propagation through the taper is given by Maxwell's curl equations that may be cast in the following form (SI units):

$$\varepsilon\varepsilon_0 \frac{\partial E_r}{\partial t} = \frac{1}{r}\frac{\partial H_z}{\partial \phi} - \frac{\partial H_\phi}{\partial z} \quad (1a)$$

$$\varepsilon\varepsilon_0 \frac{\partial E_\phi}{\partial t} = \frac{\partial H_r}{\partial z} - \frac{\partial H_z}{\partial r} \quad (1b)$$

$$\varepsilon\varepsilon_0 \frac{\partial E_z}{\partial t} = \frac{1}{r}\left[\frac{\partial}{\partial r}(rH_\phi) - \frac{\partial H_r}{\partial \phi}\right] \quad (1c)$$

$$\mu_0 \frac{\partial H_r}{\partial t} = \frac{\partial E_\phi}{\partial z} - \frac{1}{r}\frac{\partial E_z}{\partial \phi} \quad (2a)$$

$$\mu_0 \frac{\partial H_\phi}{\partial t} = \frac{\partial E_z}{\partial r} - \frac{\partial E_r}{\partial z} \quad (2b)$$

$$\mu_0 \frac{\partial H_z}{\partial t} = \frac{1}{r}\left[\frac{\partial E_r}{\partial \phi} - \frac{\partial}{\partial r}(rE_\phi)\right] \quad (2c)$$

where ε_0 and μ_0 are the permittivity and magnetic permeability of free space, respectively. The optical properties of matter (no absorption losses) are described by a real, frequency-independent dielectric function $\varepsilon = \varepsilon(r,z)$. Dispersion effects are neglected since the light paths in the media are only a few micrometres in length.

As a numerical technique, we employ a three-dimensional FDTD code for a cylindrical coordinate system which discretizes the problem in both time and space. The corresponding Yee-cell geometry is, e.g. found in Kunz & Lübbers (1993) and Taflove (1995). The space grid is composed of 200 (in r) × 12(in ϕ) × 600 (in z) cells with space increments $\Delta r = \Delta z = 10$ nm and $\Delta\phi = \pi/6$, while the time increment is 3.3×10^{-3} fs.

We consider a 10 fs Gaussian input pulse of plane-wave structure that is linearly polarized parallel to the *x*-axis and propagates along the z-direction, $E_{x,in}(t,z)$. Consequently, $E_{y,in} = E_{z,in} \equiv 0$. The pulse spectrum of $E_{x,in}(t,z)$ is centred at a vacuum wavelength $\lambda_0 = 805$ nm. In front of the fibre taper, $z < z_{input}$, $E_{x,in}$ may be written as $E_{x,in} = \hat{E}_{x,in} + \hat{E}^*_{x,in}$ with $\hat{E}_{x,in} = A_0\exp(-2\ln 2\{[t - z/c]/\tau_0\}^2 + ick_0[t - z/c])$. The real parameter A_0 is one half of the field amplitude, $\tau_0 = 10$ fs, $k_0 = 2\pi/\lambda_0$. At time $t = 0$ the peak intensity of the pulse arrives at $z = 0$. $\hat{E}^*_{x,in}$ denotes the complex conjugate of $\hat{E}_{x,in}$. The instantaneous electric energy density of the input pulse at space-time(z,t) is given by $\varepsilon_0 E^2_{x,in}$, including a high-frequency modulation factor $\cos^2\{ck_0[(t - z/c]\}$. The corresponding envelope for the electric energy density is described by $4\varepsilon_0|\hat{E}_{x,in}|^2$. The calculated squared magnitude of the *x*-component of the electric field, $|\hat{E}_x|^2$, is normalized to $A^2{}_0$, the above maximum value of $|\hat{E}_{x,in}|^2$.

In the following we show results on pulse propagation through two uncoated glass fibre probes ($\varepsilon_{Glass} = 2.25$ inside the taper) with tapers of different length (1.5 μm and 1.0 μm), termed long and short taper, respectively. The cone angles of both tapers are assumed to be identical ($\alpha = 50°$). We start with pulse propagation through the bare fibre, in the absence of a medium. Then, the propagation through fibre probes in close vicinity to a semiconductor sample will be considered.

3. Pulse propagation in uncoated fibre probes in the absence of a sample

3.1. The long taper

In the following we present results on the propagation of a 10 fs input pulse, linearly polarized along the *x*-axis (see Fig. 1), through a long glass taper of 1.5 μm length and a flat end face of $r_{exit} = 50$ nm radius. Figure 2 shows the squared magnitude of the electric field component E_x, (a) in the *x*-z-plane: $|\hat{E}_x(x, y = 0, z, t = 10 \text{ fs})|^2$ and (b) in the y-z-plane: $|\hat{E}_x(x = 0, y, z, t = 10 \text{ fs})|^2$. The plot corresponds to the time coordinate $t = 10$ fs, i.e. the approximate travelling time of the pulse from $z = 0$ to $z = z_{exit,l}$.

Two pronounced intensity peaks are seen inside the taper at $z = z_{m1}$ and $z = z_{m2}$, while close to the taper exit, $z = z_{exit,l}$, the field intensity is reduced by more than a factor of two (see cross-sections in Fig. 3). The lateral width w (FWHM) of $|\hat{E}_x|^2$ shows a minimum of about 260 nm at a distance of about 500 nm from the taper exit. Closer to the taper exit, the lateral width w increases as light leaks out of the taper sidewalls and reaches a maximum of about 390 nm at the taper exit. The two sharp peaks seen at the sidewall positions in Fig. 3(a)–(c) are a direct result of the boundary condition requirements of optical fields at an interface between different dielectric materials: in the absence of charge and current sources the field has to satisfy the boundary conditions of a continuous tangential electric field and a continuous normal electric displacement field ($D_n = \varepsilon\varepsilon_o E_n$), giving rise to discontinuity in $|\hat{F}_x|^2$ at the glass/air interface.

Corresponding cross-sections through Fig. 2(b), not shown here, indicate a similar behaviour with respect to peak heights and lateral width; however, the two sharp peaks at the sidewall positions are missing, since E_x taken along the *y*-axis, i.e. perpendicular to the polarization direction, behaves as a tangential field at the glass/air interface.

The results of these calculations are in good agreement with results presented earlier for dielectric fibre probes with

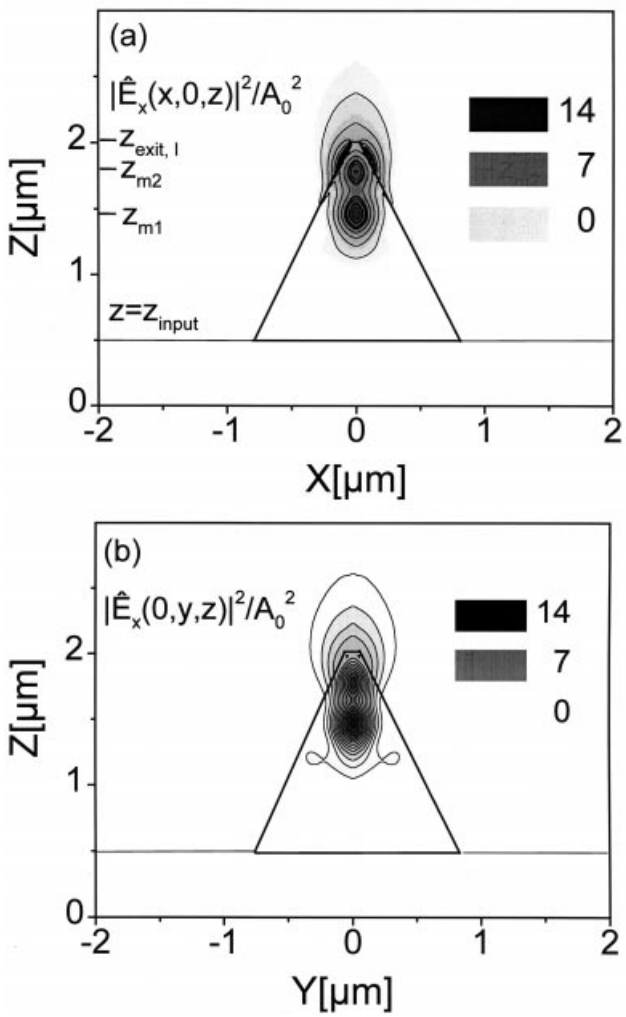

Fig. 2. Propagation of an optical pulse of 10 fs width through a long taper with a length of about 1.5 μm ($z_{exit} = z_{exit,l} \approx 2.0$ μm) and a taper radius at exit of $r_{exit} = r_{exit,l} \approx 50$ nm, see Fig. 1. The incident pulse is linearly polarized parallel to the *x*-axis. The plot shows the calculated spatial distribution of $|\hat{E}_x(x,y,z,t)|^2/A_0^2$, at t = 10 fs. The origin of the time axis, t = 0, is defined by the arrival of the peak intensity of the incident pulse at z = 0. (a) $|\hat{E}_x(x,0,z)|^2/A_0^2 \equiv |\hat{E}_x(x, y = 0, z, t = 10\text{ fs})|^2/A_0^2$ in the *x*-z plane at $y = 0$. The positions of peak intensities in the taper are indicated by $z_{m1} = 1.47$ μm and $z_{m2} = 1.79$ μm. The linear grey scale is proportional to $|\hat{E}_x(x,0,z)|^2/A_0^2$. (b) $|\hat{E}_x(0,y,z)|^2/A_0^2$ in the y-z plane at $x = 0$, i.e. perpendicular to the polarization direction.

a pointed end by Novotny *et al.* (1995). Several generalized conclusions can be drawn: $|\hat{E}_x|^2$ inside the taper reaches a minimum lateral width of about λ/2n, *n*: refractive index of the fibre. This minimum is reached at the position z_{m1}, where the ratio $q = \rho(z_{m1})/\lambda$ is about 0.3, ρ: taper radius at $z = z_{m1}$, λ: vacuum wavelength λ. This ratio is in rather good agreement with the value q ≈ 0.25 found by Buckland *et al.* (1993) for non-tapered dielectric waveguides. Towards the exit of the taper, light penetrates through the sidewalls and the field distribution increases considerably in width. Even for tapers with large opening angles, as considered here, w increases significantly beyond λ/2n.

This suggests that such long taper with pointed ends are not well suited for high spatial resolution imaging and that an improvement of the emission properties may be achieved when working with conical tapers with rather large flat end faces, cut at approximately at $z = z_{m1}$. The emission characteristics of this short taper will be considered in the following section.

3.2. The short taper

The following results correspond to such a short taper of 1 μm length and a flat end face of radius $r_{exit} = 260$ nm. Figure 4 shows the spatial behaviour of (a) $|\hat{E}_x(x, y = 0, z, t = 10\text{ fs})|^2$ in the *x*-z plane and (b) to $|\hat{E}_x(x = 0, y, z, t = 10\text{ fs})|^2$ in the y-z plane at time t = 10 fs. Contrary to Fig. 2, the lateral width of $|\hat{E}_x|^2$ at the taper exit is now reduced and the peak intensities of the E_x field appear at the

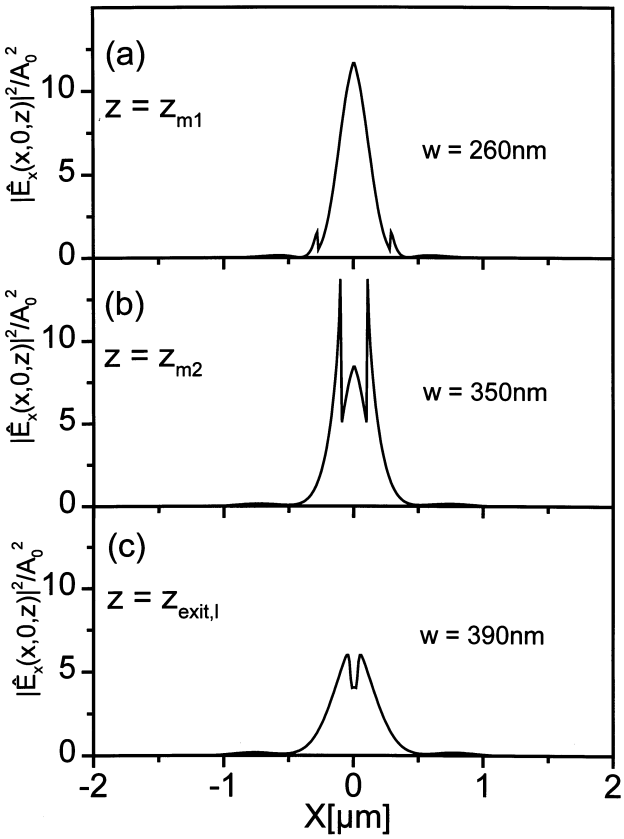

Fig. 3. Cross-sections through Fig. 2(a) at three different z coordinates:(a) $|\hat{E}_x(x,0,z_{m1})|^2/A_0^2$ at $z = z_{m1}$, the position of a strong intensity peak in the long taper. w denotes the lateral width (FWHM) of the curve. (b) $|\hat{E}_x(x,0,z_{m2})|^2/A_0^2$ at $z = z_{m2}$. (c) $|\hat{E}_x(x,0,z_{m2})|^2/A_0^2$ at $z = z_{exit,l}$, the exit of the long taper.

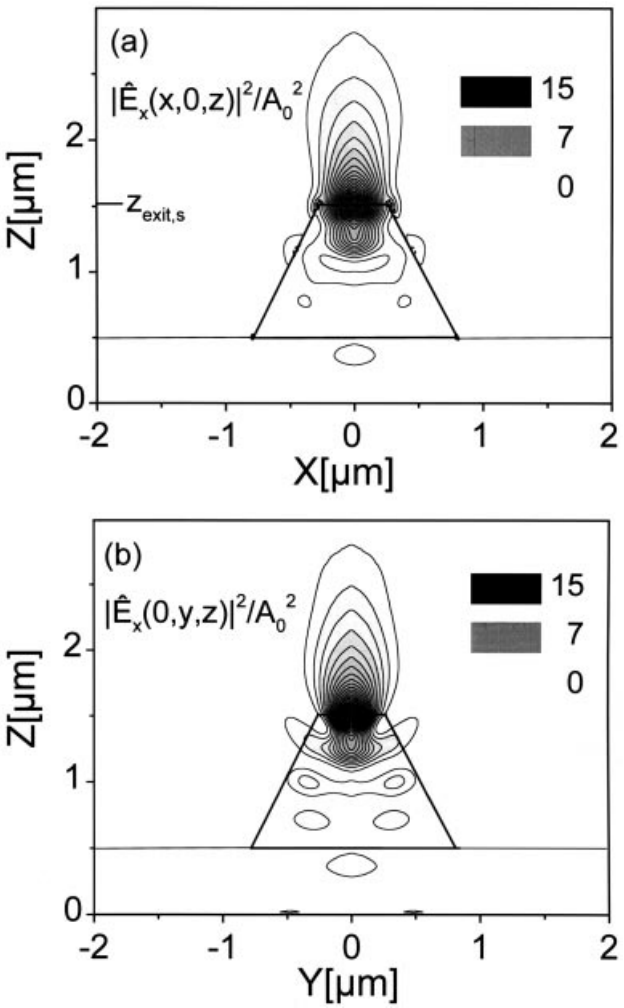

Fig. 4. Propagation of a linearly polarized optical pulse of 10 fs width through a short taper with a length of about 1.0 μm ($z_{exit} = z_{exit,s} \approx 1.5$ μm) and a taper radius at exit of $r_{exit} = r_{exit,s} \approx 260$ nm. The short taper develops from the long taper of Fig. 2 in cutting the latter at $z = z_{m1}$, the position of a strong intensity peak in the long taper. The plot shows the calculated spatial distribution of $|\hat{E}_x(x,y,z,t)|^2/A_0^2$, at $t = 10$ fs. (a) $|\hat{E}_x(x,0,z)|^2/A_0^2$. (b) $|\hat{E}_x(0,y,z)|^2/A_0^2$.

taper exit ($z = z_{exit,s}$). The lateral distribution of $|\hat{E}_x|^2$ is somewhat broader along x (Fig. 4a) than that along y (Fig. 4b) due to different guiding efficiencies in the polarization direction and perpendicular to it, similar to what is known from the propagation of p- and s-polarized waves in two-dimensional tapers (Marcuse, 1974). The plot in Fig. 4(a) shows again the discontinuous behaviour of E_x at the taper sidewall, as in the case of the long taper, Fig. 2(a). By contrast, Fig. 4(b) indicates the continuous transition of E_x along y.

Cross-sections through the plot of Fig. 4(a) at $z = z_{exit,s}$ (taper exit) and 100 nm behind it are depicted in Fig. 5. A comparison between Fig. 5(a) and 3(c) shows that the lateral width of $|\hat{E}_x|^2$ at the exit of the short taper is significantly less than that found for the long taper. Moreover, the corresponding peak height is much higher and corresponds to that in Fig. 3(a). A further fact to be noticed is an obvious difference between the areas of the $|\hat{E}_x|^2$ distributions $\sim\int |\hat{E}_x|^2\,dx$ at $z = z_{exit,s}$ and $z = z_{exit,s} + 100$ nm, see Fig. 5(a,b), which can be explained by a rather strong contribution of evanescent waves to the emitted light field. The same is true concerning the corresponding areas $\sim\int |\hat{E}_x|^2\,dy$ for the $|\hat{E}_x\ (0,y,z)|^2$ curves at $z = z_{exit,s}$ and $z = z_{exit,s} + 100$ nm (not shown). This is in contrast to preliminary results for a two-dimensional taper model (Müller & Lienau, 2000), which indicate only a minor contribution of evanescent waves.

These results clearly indicate that optimum spatial resolution with bare uncoated optical fibres is obtained with specifically designed tapers with rather large flat end faces. There is some discrepancy between these calculations and the experimental results which clearly demonstrate subwavelength resolution with uncoated tips having sharp ends. This suggests that the near-field at the taper exit is

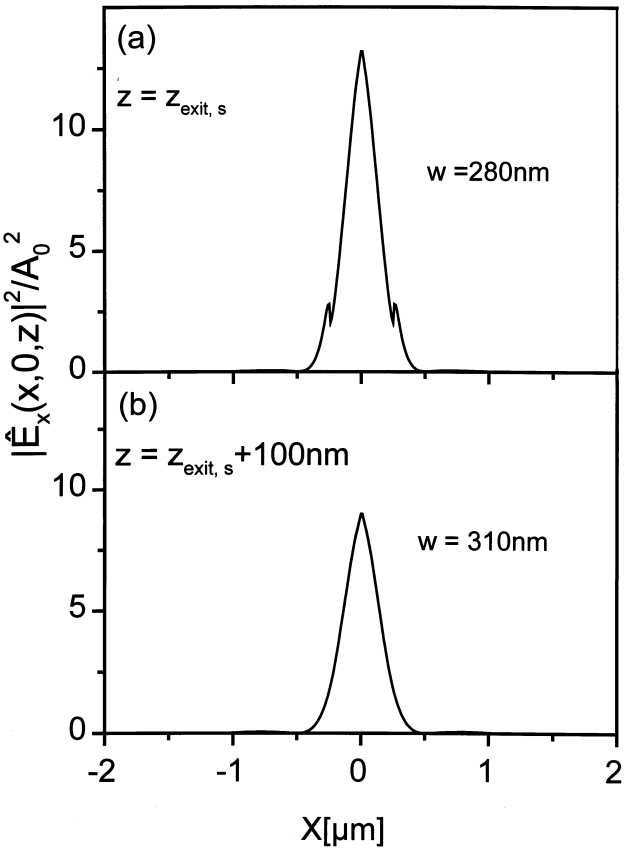

Fig. 5. Cross-sections through Fig. 4(a), at two different z coordinates, i.e. at the exit of the short taper and 100 nm behind it. (a) $|\hat{E}_x\ (x,0,z_{exit,s})|^2/A_0^2$ at $z = z_{exit,s}$. (b) $|\hat{E}_x\ (x,0,z_{exit,s} + 100\ \text{nm})|^2/A_0^2$ at $z = z_{exit,s} + 100$ nm.

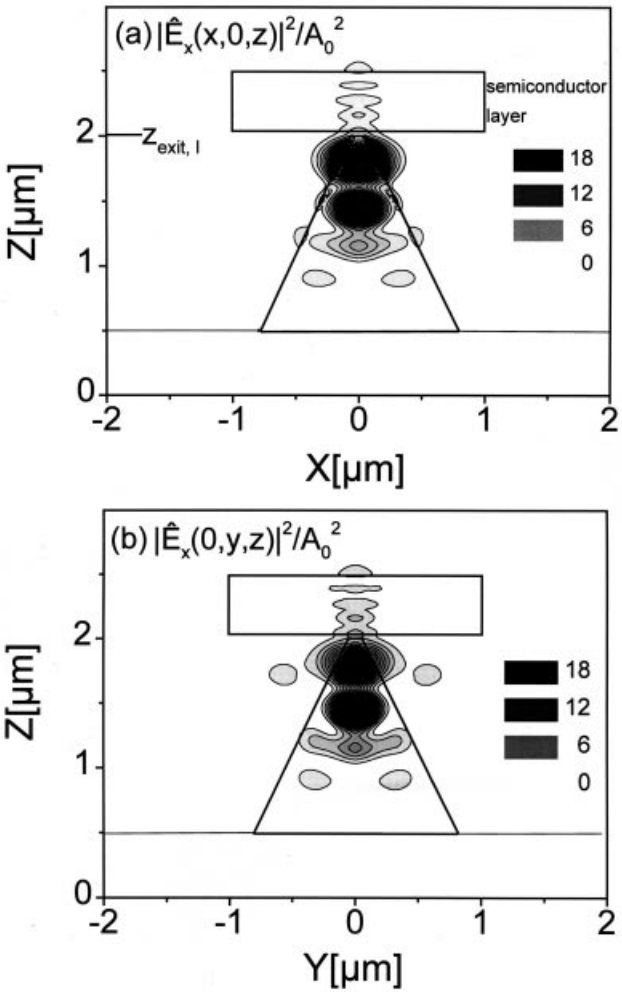

Fig. 6. Same as Fig. 2 but with a semiconductor layer set at a distance of 20 nm behind the exit of the long taper. (a) $|\hat{E}_x(x,0,z)|^2/A_0^2$ in the *x*-z plane at $y = 0$. (b) $|\hat{E}_x(0,y,z)|^2/A_0^2$ in the y-z plane at $x = 0$.

strongly modified in the presence of a high refractive medium close to the taper exit. This will be demonstrated in the next section.

4. Pulse propagation through the long taper in the presence of a sample

A 500 nm thick semiconductor layer ($\varepsilon \approx 12.25$, no light absorption) is set at a distance of 20 nm from the exit of the long taper and the pulse propagation through this structure is studied. Now we observe noticeable interference patterns in both the semiconductor medium and the taper, due to the light field that is reflected from the front and the back edges of the sample, see Fig. 6(a,b). A closer inspection shows that the peak intensities in the taper resulting from constructive interference between the input and the reflected fields are significantly higher than the highest peak intensity in the bare fibre in the absence of a medium (at $z = z_{m1}$, see Fig. 2). Directly behind the front edge of the semiconductor layer the lateral width of the interference pattern inside the sample is much smaller than the field distribution in the absence of the medium. The lateral width reaches a minimum at a short distance behind the sample edge (about 20 nm) and becomes gradually broader with increasing distance from the front edge. This can be explained as follows: due to the high refractive index of the semiconductor, light waves from the taper are collimated in the sample and then broaden due to light diffraction (Chavez-Pirson & Chu, 1999).

Figure 7 shows a cross-section through Fig. 6(a) at $z = z_{exit,l}$ (taper exit) and at $z = z_{exit,l} + 40$ nm, i.e. 20 nm behind the front edge of the semiconductor layer. Both curves show that the lateral width of $|\hat{E}_x|^2$ at the exit of the taper (w = 280 nm) and in particular inside the medium (w = 230 nm) is now considerably reduced compared to that at the exit of the bare long taper without medium. While the interference effects increase the spatial resolution obtained in this geometry, they also reduce the peak intensities at the fibre exit compared to those in the

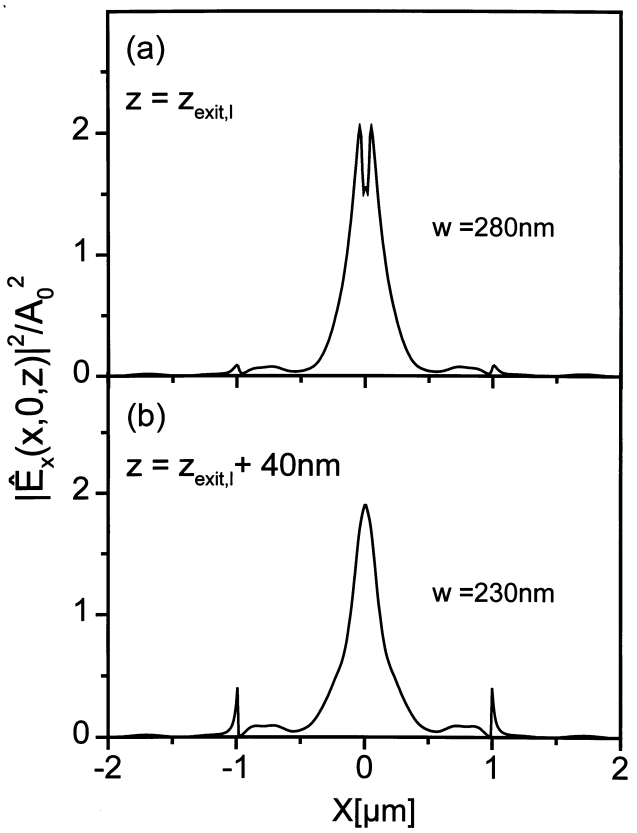

Fig. 7. Cross-sections through Fig. 6(a) at two different z coordinates: (a) $|\hat{E}_x\,(x,0,z_{exit,l})|^2/A_0^2$ at $z = z_{exit,l}$, exit of the long taper. (b) $|\hat{E}_x\,(x,0,z_{exit,l} + 40\text{ nm})|^2/A_0^2$ at $z = z_{exit,l} + 40$ nm, inside the semiconductor layer.

absence of the medium (Fig. 7). The curves show again strong discontinuities of the E_x field at the glass/air and sample/air inferfaces, respectively. The two sharp peaks at $x = \pm 1$ μm correspond to the intensity jumps at the corners of the semiconductor material while the second pair of peaks at $x = 50$ nm (Fig. 7a) are due to the glass/air interface at the taper exit. The high refractive index of the semiconductor material also has a pronounced influence on the polarization properties of the light in the near-field of the tip. Plots of $|\hat{E}_z|^2$ in the absence of a medium (not shown) indicate that in the near-field of the taper exit, the maximum of $|\hat{E}_z|^2$ is of similar magnitude as $|\hat{E}_x|^2$, whereas their spatial distributions are markedly different. Inside a high dielectric constant semiconductor material ($\varepsilon_{GaAs} \approx 12.25$), however, $|\hat{E}_z|^2$ drops drastically to about 1/150 of its magnitude outside the medium. This strong reduction in $|\hat{E}_z|^2$ is again a consequence of the boundary conditions that the optical field must satisfy at the interface of the two dielectrica (air/GaAs) and which reduces, for perpendicular incidence, $|\hat{E}_z|^2$ by a factor of $\varepsilon_{GaAs}^{-2} \approx 1/150$. This makes it very difficult to detect signatures of the z-component of the electric field in spectroscopic near-field experiments on nanostructures embedded in high refractive index materials, e.g. semiconductor quantum dots.

The above results highlight the strong influence of a high refractive index medium on the emission properties of tapered uncoated fibre probes. The presence of the medium gives rise to a significant reduction of the lateral intensity width, w, at the exit of the long taper due to the interference between the light emitted from the taper and that reflected from the sample.

Summary and conclusion

In summary, we have presented a theoretical study of the propagation of a 10 fs optical pulse through uncoated near-field fibre probes. Using a three-dimensional finite difference time domain approach (FDTD) we have studied the transmission properties of such probes for two different taper geometries and have investigated the effect of a high-refractive index dielectric medium on the near-field distribution. Our simulations show that the near-field distribution at the end of the taper is a complex function of the taper geometry and may be strongly influenced by the presence of a dielectric medium, such as, e.g. a semiconductor sample. From simulations of the bare fibre without medium, one would conclude that only tapers with a rather large flat end face of about 250 nm radius optimize the achievable spatial resolution. In the vicinity of a semiconductor sample, however, the near-field distribution inside the medium is strongly confined – even for uncoated conical tapers with sharp tips. The calculations predict inside the medium a lateral width of the near-field distribution of less than 250 nm and a nearly Gaussian-shaped transfer function for such near-field probes. These result are in good agreement with the recently reported experimental observations (Lewis *et al.*, 1998; Günther *et al.*, 1999; Intonti *et al.*, 2001) and underline the potential of such probes for high spatial resolution linear and nonlinear optical spectroscopy of semiconductor nanostructures.

Acknowledgements

We gratefully acknowledge helpful discussions with R. Grunwald and T. Guenther. We are thankful to M. Friedrich for valuable technical assistance. This work was financially supported by the European Commission (EFRE programme).

References

Adelmann, C., Hetzler, J., Scheiber, G., Schimmel, T., Wegener, M., Weber, H.B. & Lohneysen, H.V. (1999) Experiments on the depolarization near-field scanning optical microscope. *Appl. Phys. Lett.* **74**, 179–182.

Bozhevolnyi, S.I., Langbein, W. & Hvam, J.M. (1999) Polarization contrast in reflection near-field optical microscopy with uncoated fibre tips. *J. Microsc.* **194**, 500–506.

Bozhevolnyi, S.I. & Vohnsen, B. (1997) Near-field optics with uncoated fiber tips: light confinement and spatial resolution. *J. Opt. Soc. Am. B*, **14**, 1656–1663.

Buckland, E.L., Moyer, P.J. & Paesler, M.A. (1993) Resolution in collection-mode scanning optical microscopy. *J. Appl. Phys.* **73**, 1018–1028.

Chavez-Pirson, A. & Chu, S.T. (1999) Polarization effects in near-field excitation-collection probe optical microscopy of a single quantum dot. *J. Microsc.* **194**, 421–425.

von Freymann, G., Lüerssen, D., Rabenstein, C., Mikolaiczyk, M., Richter, H., Kalt, H., Schimmel, T., Wegener, M., Okhawa, K. & Hommel, D. (2000) Near-field photoluminescence imaging of single defects in a ZnSe quantum-well structure at low temperatures. *Appl. Phys. Lett.* **76**, 203–205.

von Freymann, G., Schimmel, T., Wegener, M., Hanewinkel, B., Knorr, A. & Koch, S.W. (1998) Computer simulations on near-field scanning optical microscopy: Can subwavelength resolution be obtained using uncoated optical fiber probes? *Appl. Phys. Lett.* **73**, 1170–1172.

Günther, T., Emiliani, V., Intonti, F., Lienau, C., Elsaesser, T., Nötzel, R. & Ploog, K.H. (1999) Femtosecond near-field spectroscopy of a single GaAs quantum wire. *Appl. Phys. Lett.* **75**, 3500–3502.

Hecht, B., Bielefeld, H., Inouye, Y., Pohl, D.W. & Novotny, L. (1997) Facts and artifacts in near-field optical microscopy. *J. Appl. Phys.* **81**, 2492–2498.

Hess, H.F., Betzig, E., Harris, T.D., Pfeiffer, L.N. & West, K.W. (1994) Near-field spectroscopy of the quantum constituents of a luminescent system. *Science*, **264**, 1740–1745.

Intonti, F., Emiliani, V., Lienau, C., Nötzel, R. & Ploog, K.H. (2000) Low temperature near-field luminescence studies of localized and delocalized excitons in quantum wires. *J. Microsc.* **202**, 193–201.

Kunz, K.S. & Lübbers, R.J. (1993) *The Finite Difference Time Domain Method for Electromagnetics*. CRC Press, Boca Raton, USA.

Lambelet, P., Sayah, A., Pfeffer, M., Philipona, C. & Marquis-Weible, F. (1998) Chemically etched fiber tips for near-field optical microscopy: a process for smoother tips. *Appl. Opt*. **37**, 7289–7292.

Lewis, M.K., Wolanin, P., Gafni, A. & Steel, D.G. (1998) Near-field scanning optical microscopy of single molecules by femtosecond two-photon excitation. *Opt. Lett*. **23**, 1111–1114.

Marcuse, D. (1974) *Theory of Dielectric Optical Waveguides*. Academic Press, New York.

Müller, R. & Lienau, C. (2000) Propagation of femtosecond optical pulses through uncoated and metal-coated near-field fiber probes. *Appl. Phys. Lett*. **76**, 3367–3369.

Novotny, L., Pohl, D.W. & Hecht, B. (1995) Light confinement in scanning near-field optical microscopy. *Ultramicroscopy*, **61**, 1–9.

Richter, A., Behme, G., Süptitz, M., Lienau, C., Elsaesser, T., Ramsteiner, M., Nötzel, R. & Ploog, K.H. (1997) Real-space transfer and trapping of carriers into single GaAs quantum wires studied by near-field optical spectroscopy. *Phys. Rev. Lett*. **79**, 2145–2148.

Saiki, T. & Matsuda, K. (1999) Near-field optical fiber probe optimized for illumination–collection hybrid mode operation. *Appl. Phys. Lett*. **74**, 2773–2775.

Sandoghdar, V., Wegscheider, S., Krausch, G. & Mlynek, J. (1997) Reflection scanning near-field optical microscopy with uncoated fiber tips: How good is the resolution really? *J. Appl. Phys*. **81**, 2499–2503.

Stöckle, R., Fokas, C., Deckert, V. & Zenobi, R. (1999) High-quality near-field optical probes by tube etching. *Appl. Phys. Lett*. **75**, 160–162.

Taflove, A. (1995) *Computational Electrodynamics. The Finite-Difference-Time-Domain Method.* Artech House, Boston, USA.

Toda, Y., Moriwaki, O., Nishioka, M. & Arakawa, Y. (1999) Efficient carrier relaxation mechanism in InGaAs/GaAs self-assembled quantum dots based on the existence of continuum states. *Phys. Rev. Lett*. **82**, 4114–4117.

Wu, Q., Grober, R.D., Gammon, D. & Katzer, D.S. (1999) Imaging spectroscopy of two-dimensional excitons in a narrow GaAs/AlGaAs quantum well. *Phys. Rev. Lett*. **83**, 2652–2655.